NASA/TM—2012-217740

Open Rotor Aeroacoustic Modelling

Edmane Envia
Glenn Research Center, Cleveland, Ohio

October 2012

NASA STI Program . . . in Profile

Since its founding, NASA has been dedicated to the advancement of aeronautics and space science. The NASA Scientific and Technical Information (STI) program plays a key part in helping NASA maintain this important role.

The NASA STI Program operates under the auspices of the Agency Chief Information Officer. It collects, organizes, provides for archiving, and disseminates NASA's STI. The NASA STI program provides access to the NASA Aeronautics and Space Database and its public interface, the NASA Technical Reports Server, thus providing one of the largest collections of aeronautical and space science STI in the world. Results are published in both non-NASA channels and by NASA in the NASA STI Report Series, which includes the following report types:

- TECHNICAL PUBLICATION. Reports of completed research or a major significant phase of research that present the results of NASA programs and include extensive data or theoretical analysis. Includes compilations of significant scientific and technical data and information deemed to be of continuing reference value. NASA counterpart of peer-reviewed formal professional papers but has less stringent limitations on manuscript length and extent of graphic presentations.

- TECHNICAL MEMORANDUM. Scientific and technical findings that are preliminary or of specialized interest, e.g., quick release reports, working papers, and bibliographies that contain minimal annotation. Does not contain extensive analysis.

- CONTRACTOR REPORT. Scientific and technical findings by NASA-sponsored contractors and grantees.

- CONFERENCE PUBLICATION. Collected papers from scientific and technical conferences, symposia, seminars, or other meetings sponsored or cosponsored by NASA.

- SPECIAL PUBLICATION. Scientific, technical, or historical information from NASA programs, projects, and missions, often concerned with subjects having substantial public interest.

- TECHNICAL TRANSLATION. English-language translations of foreign scientific and technical material pertinent to NASA's mission.

Specialized services also include creating custom thesauri, building customized databases, organizing and publishing research results.

For more information about the NASA STI program, see the following:

- Access the NASA STI program home page at *http://www.sti.nasa.gov*

- E-mail your question to *help@sti.nasa.gov*

- Fax your question to the NASA STI Information Desk at 443–757–5803

- Phone the NASA STI Information Desk at 443–757–5802

- Write to:
  STI Information Desk
  NASA Center for AeroSpace Information
  7115 Standard Drive
  Hanover, MD 21076–1320

NASA/TM—2012-217740

Open Rotor Aeroacoustic Modelling

Edmane Envia
Glenn Research Center, Cleveland, Ohio

Prepared for the
15th International Conference on Fluid Flow Technologies (CMFF'12)
sponsored by the Budapest University of Technology and Economics (BME)
Budapest, Hungary, September 4–7, 2012

National Aeronautics and
Space Administration

Glenn Research Center
Cleveland, Ohio 44135

October 2012

Acknowledgments

This work has been supported by the Subsonic Fixed Wing Project of the NASA Fundamental Aeronautics Program.

This report is a formal draft or working paper, intended to solicit comments and ideas from a technical peer group.

This report contains preliminary findings, subject to revision as analysis proceeds.

This work was sponsored by the Fundamental Aeronautics Program at the NASA Glenn Research Center.

Level of Review: This material has been technically reviewed by technical management.

Available from

NASA Center for Aerospace Information
7115 Standard Drive
Hanover, MD 21076–1320

National Technical Information Service
5301 Shawnee Road
Alexandria, VA 22312

Available electronically at http://www.sti.nasa.gov

Open Rotor Aeroacoustic Modelling

Edmane Envia
National Aeronautics and Space Administration
Glenn Research Center
Cleveland, Ohio 44135

Abstract

Owing to their inherent fuel efficiency, there is renewed interest in developing open rotor propulsion systems that are both efficient and quiet. The major contributor to the overall noise of an open rotor system is the propulsor noise, which is produced as a result of the interaction of the airstream with the counter-rotating blades. As such, robust aeroacoustic prediction methods are an essential ingredient in any approach to designing low-noise open rotor systems. To that end, an effort has been underway at NASA to assess current open rotor noise prediction tools and develop new capabilities. Under this effort, high-fidelity aerodynamic simulations of a benchmark open rotor blade set were carried out and used to make noise predictions via existing NASA open rotor noise prediction codes. The results have been compared with the aerodynamic and acoustic data that were acquired for this benchmark open rotor blade set. The emphasis of this paper is on providing a summary of recent results from a NASA Glenn effort to validate an in-house open noise prediction code called LINPROP which is based on a high-blade-count asymptotic approximation to the Ffowcs-Williams Hawkings Equation. The results suggest that while predicting the absolute levels may be difficult, the noise trends are reasonably well predicted by this approach.

Nomenclature

Ai, Ai'	[-] Airy function and its derivative
B	[-] rotor blade count
c_0	[m/s] ambient speed of sound
e_j	[-] unit vector component in the radiation direction
f_j	[N/m^2] blade force per unit area
G	[1/m-s] free-space, moving-medium Green's function
g_c	[-] convective phase factor
M_{0_R}	[-] medium Mach number in the radiation direction
M_{tip}	[-] rotor tip rotational Mach number
N	[rev/s] rotational speed
n_j	[-] surface unit normal vector
$p'(\underline{x},t)$	[Pa] acoustic pressure
$p'(\underline{x})$	[Pa] Fourier harmonic component of acoustic pressure
p	[Pa] blade surface pressure
$\mathcal{Q}$	[Pa] acoustic source amplitude
R	[m] distance between source and observer
S	[m^2] rotor blade surface
S_B	[m^2] reference blade surface
T_{jk}	[N/m] Lighthill stress tensor
t	[s] observer time
U_{0_j}	[m/s] medium velocity components
V	[m^3] volume exterior to the rotor blades
v_n	[m/s] normal component of blade surface velocity
$\underline{x}$, x_j	[m] observer Cartesian coordinates
$\underline{y}$, y_j	[m] source Cartesian coordinates
δ	[-] Dirac delta function
κ	[-] convective amplitude factor
ρ_0	[kg/m^3] ambient air density
τ	[s] source (i.e., retarded) time
Φ	[rad] rotor phase function
φ, φ_s	[rad] observer and source azimuthal angle coordinates
Ψ	[rad] convective phase factor
Ω	[rad/s] rotor angular speed

Subscripts:

1, 2	front and aft rotor indices
j	principal coordinate directions
s	typical source point
$\mathcal{T}$	thickness noise designator
$\mathcal{L}$	loading noise designator

Introduction

Open rotors are inherently more fuel-efficient than fans due to their very high propulsive efficiency. With the rising fuel cost and the increasing restrictions on carbon emissions (CO_2 emissions are directly related to fuel burn) there is renewed interest in developing open rotor systems for commercial aviation applications.

The fuel burn advantage of open rotor propulsion systems was convincingly demonstrated in the past (for example, in the late 1980s and early 1990s as part of a NASA effort called the Advanced Turboprop Project (Ref. 1)). A model scale open rotor developed by NASA and General Electric (GE) under that project and the subsequent engine demonstrator developed by GE, called the unducted fan (UDF), are shown in Figure 1. At that time, some of the fuel burn margin of UDF was traded off in order to meet the noise regulations of the time. Changes to the design paradigm (e.g., blade count increase and tip speed reduction) and the advent of the high-fidelity three-dimensional aerodynamic simulation tools have now made it possible to design open rotor systems that can meet the current noise regulations (which are more stringent than the 1990s rules) without giving up any of their fuel burn advantage.

As a result, both the United States and Europe have been pursuing the development of the next generation open rotor propulsion systems. In particular, in the U.S., a joint effort between NASA and GE Aviation was initiated to investigate the aerodynamic and acoustic performance of modern blade designs. An important element of this effort has been the assessment of existing tools for predicting the aerodynamic and acoustic performance of open rotors. For that purpose a baseline, vintage 1990s, blade design called the historical blade set (also known as F31/A31) was selected for evaluating various prediction tools. F31/A31 has 12 front rotor blades and 10 aft rotor blades.

Comprehensive aerodynamic, flowfield, and acoustic data sets were acquired in the NASA wind tunnels for a ~0.65 m diameter sub-scale model of this blade set. The test campaign included both low speed testing in the NASA 9- by 15-foot (i.e., 2.7 by 4.6 m) wind tunnel to investigate the aero/acoustic performance at operating conditions in the approach to take-off range as well as high speed testing in the NASA 8- by 6-foot (i.e., 2.4 by 1.8 m) wind tunnel to analyse the aerodynamic performance in the speed range between climb and cruise conditions (Ref. 2). Data was acquired in an un-installed configuration, as well as at angles of attack and with a generic pylon for some conditions. In all, a sizable matrix of rotor blade setting angles, tip speed, and tunnel Mach number combinations were investigated. In this paper, the focus is on a small subset of the un-installed (zero angle of attack) configurations that were run in the low speed regime at one set of blade angles, and one tunnel Mach number. The testbed F31/A31 open rotor is shown installed in the NASA 9- by 15-foot wind tunnel in Figure 2.

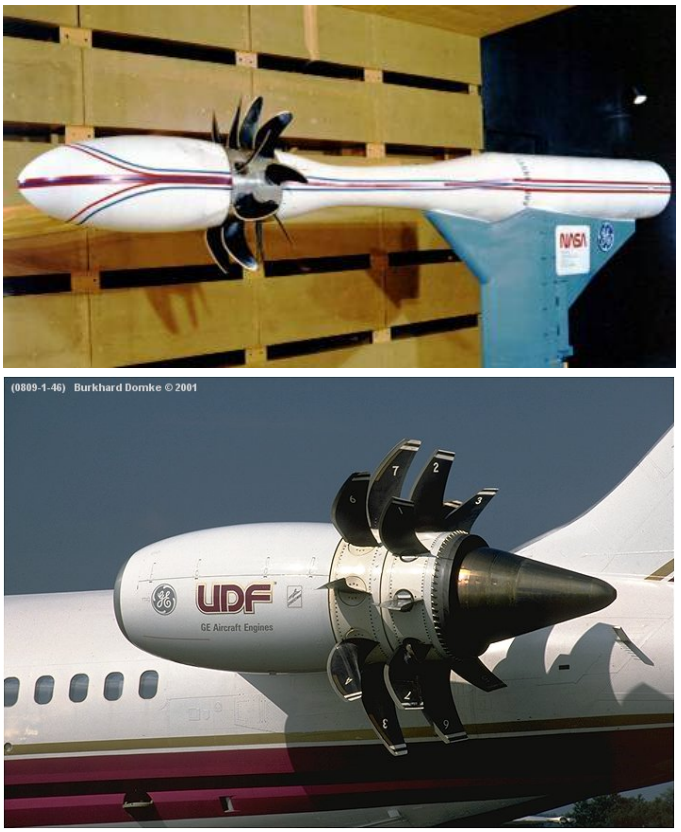

Figure 1.—Top: GE/NASA Unducted Fan (UDF) model installed in NASA wind tunnel (1985). Bottom: GE UDF engine demonstrator installed on the MD-80 testbed aircraft (1987). UDF had equal blade counts, eight each on the front and aft rotors.

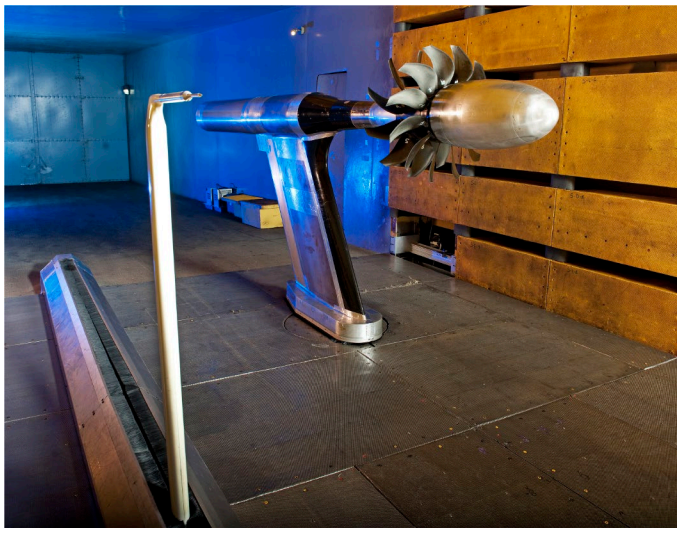

Figure 2.—Model scale F31/A31 historical baseline blade set shown installed in the NASA 9- by 15-foot wind tunnel (2010). The front rotor of F31/A31 has 12 blades and its aft rotor has 10 blades. Traversing inflow microphone system used for sideline acoustic pressure measurements is visible on the left.

Aeroacoustic Modelling

The methodologies for predicting open rotor noise can be categorized into three main groups. The most basic approaches are empirical in nature which, as the name suggests, are based on curve fits to database(s) of measured noise as a function of the geometry and operating parameters of open rotors. Once developed these are relatively easy to use and are often employed for trend studies in the early phases of the design process. Their shortcoming, however, is that they cannot be reliably used to predict noise for configurations or operating conditions that are well outside of the envelope of the databases used for developing the models in the first place.

On the opposite end of the spectrum are the high-fidelity numerical approaches that can be used to solve for the unsteady flowfield of the open rotor and include, as part of the solution, the noise field of interest. These types of methods typically require sizable computational resources due to the huge differences in the flow scales involved. For example, whereas the background flow pressure levels may be at the ambient atmospheric level, the acoustic perturbation levels of interest are easily three to four orders of magnitude smaller. This disparity necessities highly resolved grids nearly everywhere in the domain of interest thus driving up the computer memory and computational time requirements.

It is in the middle ground between these two extremes where most of the current state of practice resides. Typically, the issue of scale disparity is circumvented by linearizing the equations of motion thus separating the nonlinear aerodynamic field from the linear acoustic field. In the linearized methods, the nonlinear aerodynamic field is specified, measured, or computed *a priori* and is introduced as source terms in the linearized equations governing the acoustics. Computational fluid dynamics (CFD) is most often used for that purpose. Once this input information is specified, the acoustic equations can be solved to estimate the acoustic field. The solution could be affected by solving the linearized equations numerically, but most often the solution is obtained using the Lighthill's acoustic analogy approach whose extension to the moving surfaces is the Ffowcs-Williams Hawkings (FW-H) equation. This equation describes the acoustic field as temporal and spatial integrals over aerodynamic source regions of interest (e.g., rotor blades and the surrounding flowfield). The approach used in this paper for predicting open rotor noise is based on an asymptotic approximation to the FW-H equation with the necessary aerodynamic input obtained via a commercial CFD code.

Acoustic Modelling

The FW-H equation, see Equation (1a), is an exact formal solution of the general equations of motion accounting for all of the underlying physics. It expresses the sound field $p'(\underline{x},t)$ as integrals of the aerodynamic source distributions. These source distributions are traditionally called the thickness, loading, and quadrupole sources, corresponding to the three terms on the right hand side of Equation (1a), respectively. v_n is the normal velocity of the blade, $f_j dS$ is the blade force, and T_{jk} (the Lighthill stress tensor) represents the fluctuating stresses in the flowfield surrounding the rotor blades. Here only the inviscid parts of f_j and T_{jk} are implied, since viscosity does not significantly contribute to the open rotor noise field. In fact, we shall neglect the contribution of the quadruple source entirely since the focus of this paper is on the low speed operating conditions for which the quadrupole source does not significantly contribute to the noise field.

$$p'(\underline{x},t) = -\int_{-\infty}^{\infty}\int_{S(\tau)} \rho_0 v_n(\tau)\frac{D_0 G}{D\tau} dS(\underline{y})d\tau + \int_{-\infty}^{\infty}\int_{S(\tau)} f_j(\tau)\frac{\partial G}{\partial y_j} dS(\underline{y})d\tau + \int_{-\infty}^{\infty}\int_{V(\tau)} T_{jk}(\tau)\frac{\partial^2 G}{\partial y_j \partial y_k} d\underline{y}d\tau \qquad (1a)$$

$$\frac{D_0}{D\tau} = \frac{\partial}{\partial\tau} + U_{0_j}\frac{\partial}{\partial y_j}$$

In this equation, G is the free-space, moving-medium Green's function given by

$$G(\tau) = \frac{1}{4\pi\kappa R}\delta\left(t - \tau - g_c R/c_0\right)$$
$$g_c(\tau) = \frac{1}{\beta_0^2}\left(\kappa - M_{0_R}\right)$$
$$\kappa(\tau) = \sqrt{{M_{0_R}}^2 + \beta_0^2}, \quad M_{0_R}(\tau) = M_{0_j} e_j \qquad (1b)$$
$$e_j(\tau) = \frac{\left(x_j - y_j\right)}{R}, \quad R(\tau) = \left|\underline{x} - \underline{y}(\tau)\right|$$
$$\beta_0 = \sqrt{1 - M_{0_j}^2}, \quad M_{0_j} = \frac{U_{0_j}}{c_0}$$

where g_c and κ are factors that embody the effects of medium convection on the propagation time $g_c R/c_0$ and spherical spreading rate $1/R$. Where applicable, the explicit dependence of various variables on the source time τ is indicated. Assuming that the geometry of the rotor blades, their loading distributions, and the surrounding flow field are known, the integrals in Equation (1a) can be explicitly integrated to provide an estimate of the sound field generated by the open rotor.

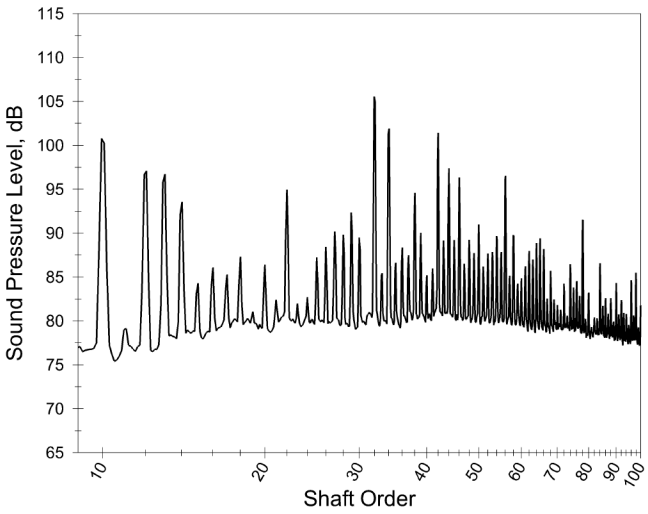

Figure 3.—Sound pressure level (SPL) of the model scale F31/A31 blade set 1.524 m away and 90° from the open rotor axis. The SPL is plotted versus the multiples of the open rotor shaft frequency (i.e., shaft orders). The shaft frequency is 107.3 Hz for this case.

While in principal, Equation (1a) can be computed explicitly by carrying out the indicated spatial and temporal integrals using appropriate quadrature schemes, e.g., see Farassat (Ref. 3) and Brentner (Ref. 4), most often this equation is tackled in the frequency domain and by assuming that the observer is in the farfield. This assumption results in considerable simplification of the integrands in Equation (1a) leading to semi-analytic formulas. See, for example, the models due to Hanson (Ref. 5) and Parry (Ref. 6). The strategy used in this paper for carrying out the integrals in Equation (1a), while frequency-domain based, does not require such simplification and the resulting formulas are valid for any observer (in the nearfield or in the farfield).

Specifically, the formulas used in this paper are extensions of the single rotation ones developed in Reference 7 to account for the counter rotation configuration. The main difference between the single and counter rotation versions is the treatment of the loading noise. Another feature of the extended theory is that, owing to the linearity of the sound field, the analysis is carried out for each rotor separately and the resulting sound fields superimposed at the end. The derivation of the working expressions will closely follow that described in Reference 7 and will use essentially the same notation. The details of the derivation are included in the Appendix A and only final formulas are given here.

Owing to the dominance of the open rotor spectra by tone noise (see Fig. 3), in this study the modelling is focused on the tonal component of the noise spectrum. Let the blade counts and rotational speeds of the two rotors be denoted, respectively, by $B_1 \& B_2$ and $N_1 \& N_2$, where the subscript "1" refers to the front rotor. It should be noted that the open rotor blade counts or the rotational speeds of the two rotors need not (and frequently are not) equal. The tonal acoustic field of the front rotor is given by the following formula

$$4\pi p'(\underline{x},t) = \sum_{m=-\infty}^{\infty} p'_{\mathcal{T}_m}(\underline{x}) e^{-imB_1\Omega_1 t} + \sum_{m=-\infty}^{\infty}\sum_{k=-\infty}^{\infty} p'_{\mathcal{L}_{m,k}}(\underline{x}) e^{-i(mB_1\Omega_1 + kB_2\Omega_2)t} \tag{2a}$$

where $p'_{\mathcal{T}_m}$ is the thickness noise harmonic amplitude given by the expression

$$p'_{\mathcal{T}_m}(\underline{x}) \simeq iB_1 \sum_{n=1}^{2} \int_{S_{B_1}} e^{mB_1(\mu_{\mathcal{T}} - i\Psi_{\mathcal{T}})} \times \left\{ d_{0,n} \frac{Ai\left[(mB_1)^{2/3}\gamma_{\mathcal{T}}^2\right]}{(mB_1)^{1/3}} + d_{1,n} \frac{Ai'\left[(mB_1)^{2/3}\gamma_{\mathcal{T}}^2\right]}{(mB_1)^{2/3}} \right\} ds \tag{2b}$$

$$\Psi_{\mathcal{T}} = \frac{1}{\beta_{0_1}} M_{\mathrm{tip}_1} M_{0_1} \chi_s + \varphi_s - \varphi$$

with $\Omega_1 = 2\pi N_1$ denoting the angular frequency of the front rotor and $M_{\mathrm{tip}_1} = \Omega_1 R_{\mathrm{tip}_1} / c_0$ its tip rotational Mach number. $\gamma_{\mathcal{T}}$ and $\mu_{\mathcal{T}}$ are defined by Equation (A.11) in the Appendix. The Airy function Ai and its derivative Ai' give an accurate asymptotic approximation to the integral over τ appearing in the Equation (1a). That integral represents the radiation efficiency of a source point over one period of its revolution about the axis of the rotor. Thus, the expression inside the curly bracket provides a closed form formula for the radiation efficiency of a given source point. Note that, Equation (2a) indicates that thickness noise is produced at the harmonics of the front rotor blade passing frequency $B_1\Omega_1$. The larger the parameter mB_1 is, the more accurate this approximation becomes.

Similarly, the loading noise harmonic amplitude $p'_{\mathcal{L}_{m,k}}$ is given by

$$p'_{\mathcal{L}_m}(\underline{x}) \simeq iB_1 \sum_{n=1}^{2} \int_{S_{B_1}} e^{(mB_1 - kB_2)(\mu_{\mathcal{L}} - i\Psi_{\mathcal{L}})} \times$$

$$\left\{ d_{0,n} \frac{Ai\left[(mB_1 - kB_2)^{2/3} \gamma_{\mathcal{L}}^2 \right]}{(mB_1 - kB_2)^{1/3}} + \right.$$

$$\left. d_{1,n} \frac{Ai'\left[(mB_1 - kB_2)^{2/3} \gamma_{\mathcal{L}}^2 \right]}{(mB_1 - kB_2)^{2/3}} \right\} \qquad (2c)$$

$$\Psi_{\mathcal{L}} = \frac{1}{\beta_{0_1}} \eta_{\mathrm{CRF}} M_{\mathrm{tip}_1} M_{0_1} \chi_s + \varphi_s - \varphi$$

$$\eta_{\mathrm{CRF}} = \frac{mB_1 + kB_2 \Omega_2 / \Omega_1}{mB_1 - kB_2}$$

where $\Omega_2 = 2\pi N_2$ is the angular frequency and $B_2\Omega_2$ the blade passing frequency of the aft rotor. As before, $\gamma_{\mathcal{L}}$ and $\mu_{\mathcal{L}}$ are defined by Equation (A.11) in the Appendix. Equation (2c) shows that, in general, loading noise is produced at the frequency combinations $mB_1\Omega_1 + kB_2\Omega_2$ where m is called the acoustic harmonic and k the loading harmonic. For $k = 0$, Equation (2c) reduces to the isolated rotor loading noise formula derived in Reference 7. Note that the loading noise harmonic amplitude is a function of the difference parameter $mB_1 - kB_2$. As will be discussed in the results section this parameter plays a crucial role in determining the magnitude of the various loading noise tones.

Nearly identical expressions for the aft rotor tone noise field can be derived but with (B_1, Ω_1) pair interchanged with (B_2, Ω_2) pair in Equations (2a) to (2c). Once the contributions from both rotors have been computed, the resulting sound fields can be superimposed to estimate the tonal sound field of the counter-rotating open rotor. Equations (2a) to (2c), and their counterpart for the aft rotor, are the working expressions used for computing the tone noise of F31/A31 blade set reported here. These expressions were incorporated into an existing NASA Glenn Research Center propeller noise code called LINPROP to predict the tone noise of open rotors. The original LINPROP code was developed in early 1990s based on the single rotation theory described in Reference 7.

Aerodynamic Calculations

The computational tool used in this paper for the aerodynamic calculations is the commercial CFD software package FINE/Turbo developed by NUMECA International[1] FINE/Turbo is a turbomachinery CFD simulation software package with integrated meshing and post-simulation analysis tools. It is a structured, multi-block, unsteady Navier-Stokes solver which offers several solution algorithm choices along with several acceleration strategies. The simulations can be run in full unsteady mode though this could be quite resource intensive. To reduce the computational time requirements for the time-dependant simulations, FINE/Turbo can also be run in the nonlinear harmonic (NLH) mode (Ref. 8) which solves for a finite number of the blade passing frequency harmonic components of the time-dependent solution, but ignores all the other unsteady components. This is a targeted approach focusing on the relevant frequency content of the underlying unsteady flow. The net result is a very significant reduction in the computational time requirements. This is the approach employed in this paper for the purpose of computing the aerodynamic response. In results to be presented later in the paper, the blade loading perturbation pressures associated with the first three harmonics of the blade-passing frequency for each rotor were retained in addition to the blade mean pressure field. Only three loading harmonics were chosen to keep the computational cost reasonable while still ensuring that the relevant tones up to 50$^{\mathrm{th}}$ shaft order could be modelled (see Fig. 3). The implications of this choice will become clear when the acoustic predictions are discussed later in the paper.

The FINE/Turbo computational domain used in generating the results presented here includes one passage each of the two blade rows and their associated ancillary domains like the spinner, hub, farfield, etc. (see Fig. 4). The total mesh size is slightly over 27.1 million grid points with the farfield boundary set seven tip radii away. The computations were run in parallel mode and depending on the particular simulation, the domain was partitioned either into 39 or 42 blocks to achieve optimum computational load balance.

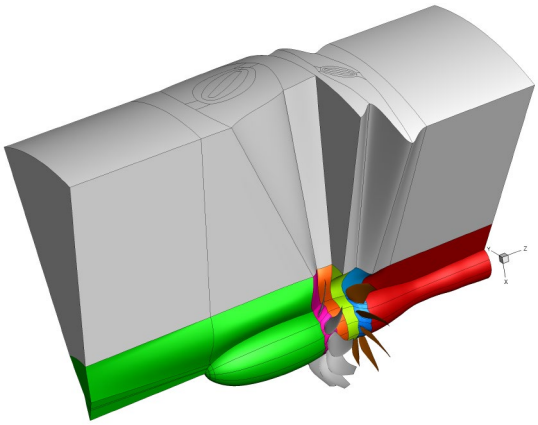

Figure 4.—The computational domain and grid blocks used for nonlinear harmonic FINE/Turbo simulations. Block regions are distinguished by different colors with the “farfield” blocks shown in gray.

[1] Additional information regarding FINE/Turbo software package may be found at http://www.numeca.com.

TABLE 1.—ROTOR RPMS CONSIDERED IN THIS STUDY

Case	Front rotor, rpm	Aft rotor, rpm
1	4620	4620
2	5268	5268
3	5551	5551
4	6068	6068
5	6303	6303
6	6436	6436

In total, six tip speeds were considered ranging from the approach rpm to the nominal takeoff rpm. Table 1 shows the rotor tip speeds modelled in this paper. All cases considered had equal rpms on the front and aft rotors. The nominal blade setting angles were 40.1° for the front rotor and 40.8° for the aft rotor in all cases. The tunnel Mach number (i.e., open rotor "forward flight speed") was also fixed at 0.2. As was mentioned in the introduction, these cases represent a small subset of a very large matrix of configurations for which aerodynamic and acoustic data was acquired in the wind tunnel tests.

The starting point for the simulations was the highest tip speed condition, which was converged first. It took a total of 4000 iterations (3000 of them in NLH mode) to converge the solution. The maximum residual, thrust, torque, and pressure ratio had all settled after 3500 iterations, but the simulation was run another 500 iterations to ensure complete convergence. The acoustic calculations based on the 3500 and 4000 iteration solutions were nearly identical also. Once convergence had been achieved for this rpm, the next lower tip speed condition was run starting with this converged solution as the initial solution. Typically, it took 2500 iterations to achieve full convergence. The process was repeated for the next lower tip speed condition until all cases were computed. The simulations typically used between 14 and 16 cores of a 48-core compute node that is part of a NASA Glenn computer cluster each compute node of which has 128 GB of RAM.

Figures 5 and 6 show comparisons of total thrust and torque ratio predicted by FINE/Turbo against the wind tunnel data. The agreement for thrust is quite good with an average discrepancy of 1.6 percent. The torque ratio comparison is only fair with an average error of roughly 9 percent. It should be noted that no tweaks were performed to adjust the blade angle, rotor tip speeds, or the tunnel Mach number to achieve a better match with the data. In other words, the simulations represent true "predictions".[2]

Figure 7 shows the contours of predicted magnitude of the mean and first blade passing frequency harmonic of the static pressure distribution on the front and aft blade rows as well as on the hub. Note the change in scale of the contour levels between the mean and perturbation contours. A close examination of the levels on the front and aft row shows that,

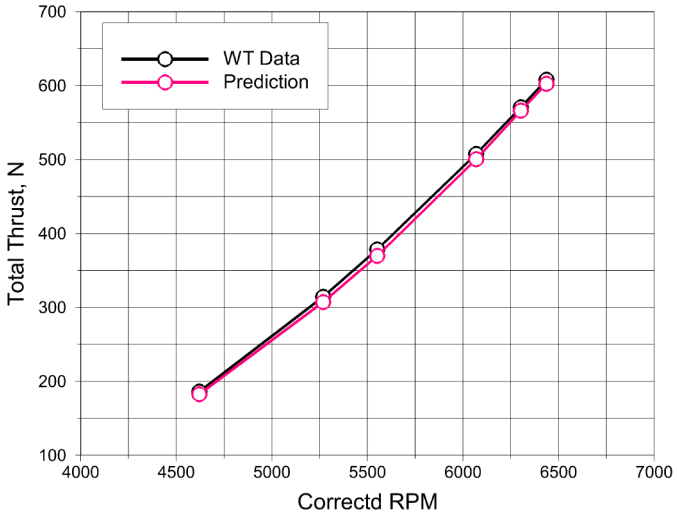

Figure 5.—Measured and predicted F31/A31 rotor thrust. Combined thrust produced by both rotors is plotted.

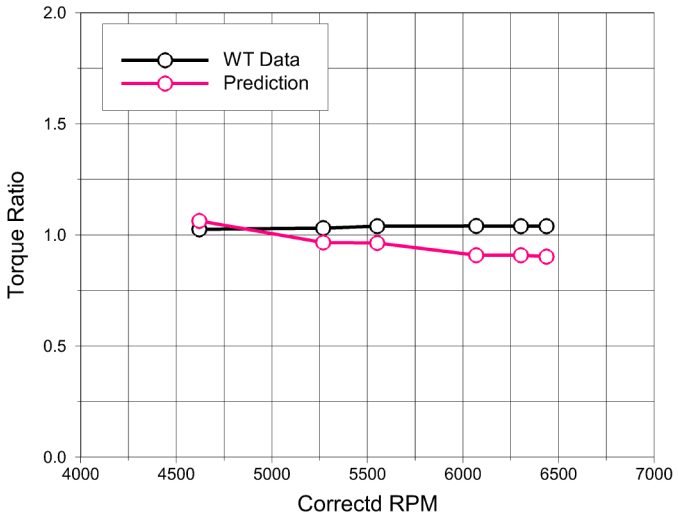

Figure 6.—Measured and predicted F31/A31 rotor torque ratio.

while the mean loading levels on the front and aft rotors are comparable, there is a significant difference between the magnitudes of perturbation pressures on the two blade rows. The aft row clearly experiences much higher levels of pressure fluctuations owing to the impingement of the wakes of the front rotor, whereas the front rotor is only weakly affected by the potential field of the aft rotor. Another noteworthy feature is that the suction side perturbations are larger than the pressure side. The second and third harmonic pressure perturbations show similar trends to the first harmonic component, but they are smaller than the first harmonic component by roughly a factor of two and four, respectively.

[2] The blade shapes at the max climb condition supplied by GE were used at all speeds studied here. Thus, the small variations in the hot blade shape due to the changes in centrifugal force as a function of rpm difference from the max climb condition were ignored.

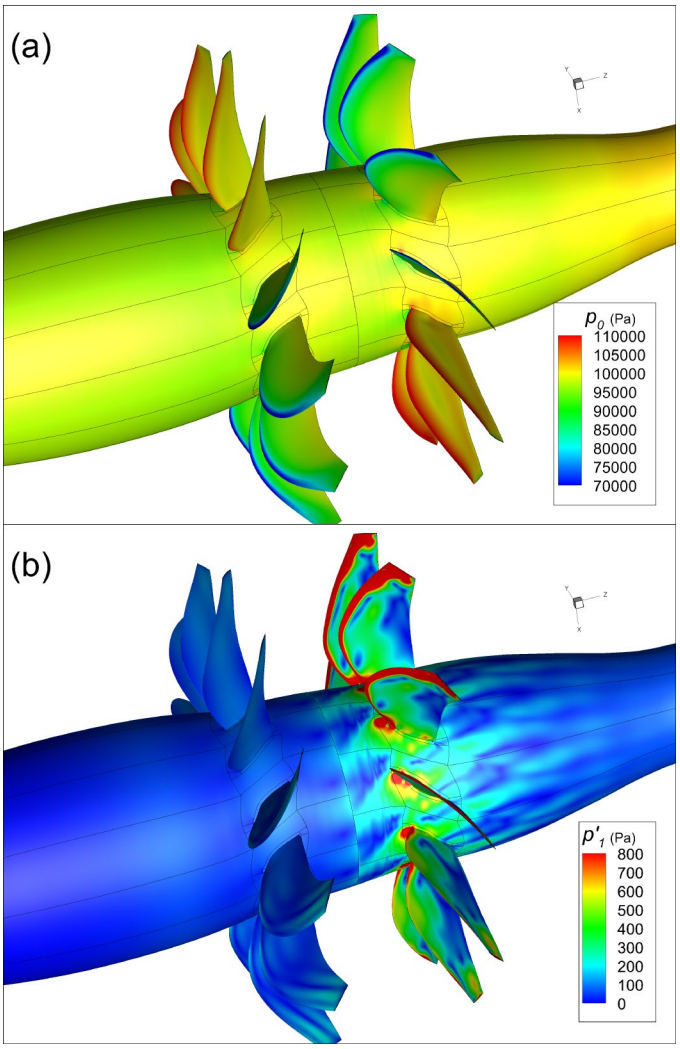

Figure 7.—Contours of predicted pressure distributions on the hub and rotor blades for F31/A31. (a) shows the mean pressure level and (b) the blade passing frequency harmonic level.

By plugging the blade geometries and aerodynamic pressure distributions for each rotor into the Equations (2b) to (2c) the harmonic amplitudes of the thickness and loading tone noise were calculated and combined to estimate the sound field of F31/A31. The noise prediction results are discussed in the next section.

Acoustic Predictions

The modified LINPROP code was run for all of the tip speed conditions considered in this study. The calculations were performed for observer (i.e., microphone) positions that are located in a horizontal plane containing the open rotor axis and on a sideline parallel to the axis of the open rotor and 60 in. (i.e., 1.524 m) displaced from it. This layout duplicates

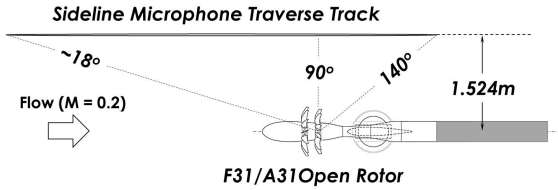

Figure 8.—Sketch of the F31/A31 open rotor testbed and the sideline traversing microphone track as they were installed in the 9- by 15-foot wind tunnel. Acoustic data was acquired at a total of 18 microphone stops between the observer angles 18° and 140°.

exactly the test arrangement in the NASA 9- by 15-foot wind tunnel shown in the sketch in Figure 8.

During the test, the sideline acoustic data was acquired at 18 microphone positions ranging between 18° and 140° from the open rotor axis as shown in the figure. The data was acquired using a traversing inflow microphone (see Fig. 2). Spectral data was computed from 15-sec long time series acquired at 200 kHz sampling rate with a 2^{14} point FFT resulting in a frequency bin width of 12.2 Hz. Consequently, the measured tone energy is spread across multiple bins (see Fig. 3). Therefore, to compare the measured levels to the predicted ones (which have an effective bin width of zero), it was necessary to sum the tone energy in the bins over which the tone is spread for the measured data.

As for the predictions, the loading component dominates the total level in all cases, hence only the predicted total is presented here. In any case, the experimental data cannot be parsed into constituent thickness and loading components. Also, while the data was acquired at 18 observer angles, the predictions were computed on a finer angular resolution of 51 observer angles to ensure that the nuances of the tone directivities were well captured. Lastly, given the number of the rpm and tone combinations, only highlights are presented here.

Figure 9 shows a representative comparison of the predicted tone sound pressure level (SPL) from the LINPROP code with the measured level for the highest tip speed (i.e., 6436 rpm) at the broadside microphone location (i.e., observer angle of 90°). Predictions for the tones in the range from approximately 1 to 5.3 kHz are shown (shaft frequency for this tip speed is 107.3 Hz). This is because, the FINE/Turbo simulations include the mean and only the first three blade passing frequency harmonics of the blade pressure loading for each row, which determines how many open rotor tones could be calculated based on the relationship $\left|mB_1\Omega_1 \pm kB_2\Omega_2\right|$. Therefore, the noise predictions are restricted to the tones for which the loading harmonic k does not exceed 3.

The tones are labelled based on whether their origin is the front rotor, aft rotor, or if they are produced as a result of the interaction of the two. The frequency for each tone is given by $\left|mB_1\Omega_1 \pm kB_2\Omega_2\right|$ where $m,\ k = 0,1,2,3$.[3] The predicted levels

[3] m=k=0 does not result in an acoustic tone.

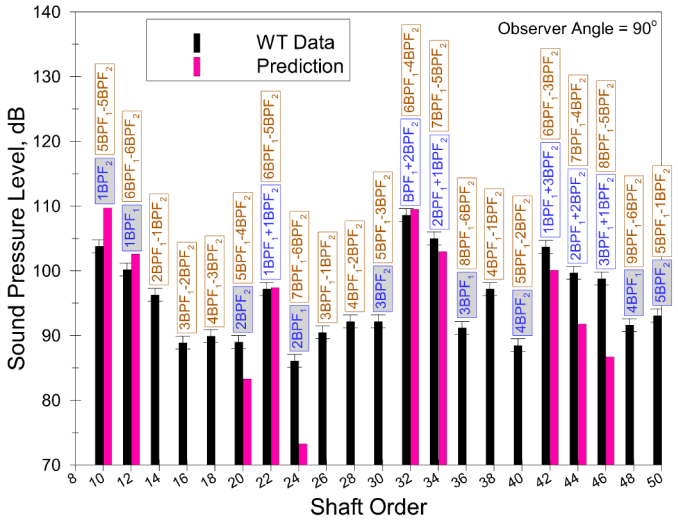

Figure 9.—Comparison of measured and predicted tone SPL at the broadside microphone location (i.e., observer angle 90°) at 6436 rpm. Tones are labeled according to their origin (i.e., front rotor tones, aft rotor tones, or interaction tones). The labels are color coded according to whether the tones are based on sum (blue) or difference (brown) combinations.

include the complex conjugate contributions corresponding to the associated negative frequencies $-\left|mB_1\Omega_1 \pm kB_2\Omega_2\right|$. Before discussing the data-theory comparisons, it is important to note the following in order to better understand the comparisons.

As indicated in Figure 9, most tones can be produced by either the sum or difference frequency combinations. In fact, while there is only one sum combination for a given tone, there are infinitely many difference combinations possible. However, tones corresponding to virtually all frequency difference combinations have extremely low radiation efficiencies and do not contribute to the tone SPL in a significant way. This is most easily seen by examining the terms inside the curly bracket in Equation (2c).

Note that since for a given frequency combination $\left|mB_1\Omega_1 \pm kB_2\Omega_2\right|$, the tone amplitude is a function of the index combination $\left|mB_1 \mp kB_2\right|$, there can be substantial difference in the radiation efficiency of the sum and difference tones. To elucidate the point, let's contrast two tones, one with the frequency $\left|12\Omega_1 + 10\Omega_2\right|$ and the other with the frequency $\left|12\Omega_1 - 10\Omega_2\right|$. The amplitudes of these two tones according to Equation (2c) will be functions of the index combinations $\left|12+10\right|$ and $\left|12-10\right|$, respectively. Since, *Ai* and *Ai′* decay rapidly as their arguments increase, the amplitude of the sum tone will far exceed the amplitude of the difference tone. The plot in Figure 10 depicts the point graphically. The plot shows the dependence of the terms in the curly bracket in Equation (2c) on the parameter $\left|mB_1 - kB_2\right|$ for a source on the tip of the blade. The terms are each normalized by their value for zero argument and plotted on a logarithmic scale.

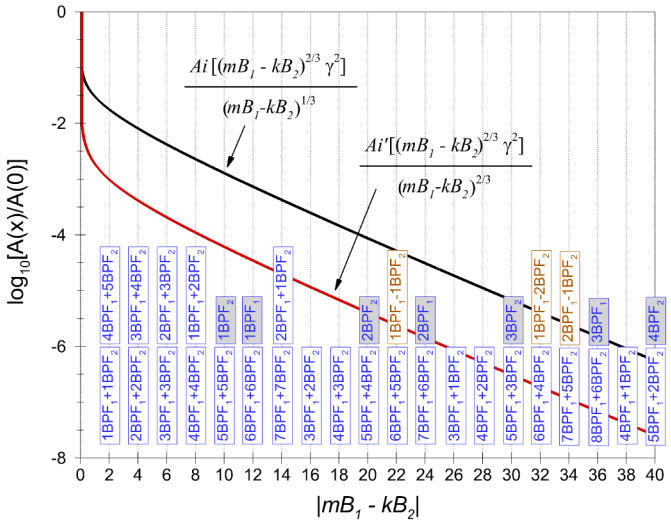

Figure 10.—Radiation efficiency of sum and difference tones as a function of the index $\left|mB_1 - kB_2\right|$.

A number of tones for which the parameter $\left|mB_1 - kB_2\right|$ falls in the range 0 to 40 are identified on the abscissa. Tones whose frequencies are above 14 kHz are not noted since beyond that limit no discernible tones are detectable above the broadband level in the measured spectra. Note the rapid fall of the *Ai* and *Ai′* as their arguments increase. It is easy to see from this plot that sum tones have far higher radiation efficiencies than do the difference tones. In fact, there are only three difference tones in the range plotted. The radiation efficiencies of higher order difference tones are effectively negligible.

Another notable aspect of this plot is that it shows that the radiation efficiencies of several interaction (sum) tones are significantly higher than the radiation efficiencies of the individual rotor blade passing tones (i.e., BPF_1 and BPF_2). As a result, even though the magnitude of the blade loading's higher harmonics, which drive the interaction tones, are much smaller than the mean loading, which drives the blade passing tones, their comparatively much higher radiation efficiencies compensate for their source amplitude deficit (recall Fig. 7) thus making their levels, especially those for the low order interaction tones, on par or even higher than the blade passing frequency tone levels. Finally, it should also be noted that the higher harmonic tones of the individual rotors (i.e., nBPF$_1$ and nBPF$_2$) also have comparatively smaller radiation efficiencies and thus are expected to fall off rapidly in amplitude as seen in this plot.

Returning to Figure 9, note that the low order interaction tones $1BPF_1$+$1BPF_2$, $2BPF_1$+$1BPF_2$, and $1BPF_1$+$2BPF_2$, are well predicted by the LINPROP code with discrepancies of 1 dB or less, when considering the experimental uncertainty in the measured levels which is ±1 dB. The next set of interaction tones, $3BPF_1$+$1BPF_2$, $2BPF_1$+$2BPF_2$, and $1BPF_1$+$3BPF_2$, show larger discrepancies when compared with the measured levels and the discrepancy grows as the

tone order (i.e., its frequency) increases. Since, as mentioned earlier, the interaction tones are driven by the harmonics of the unsteady loading on the blades, it is likely that to predict higher order tones more computational grid resolution may be needed to achieve better accuracy of the blade pressure loading harmonics.[4]

As for the individual rotor tones, the theory over-predicts the blade passing frequency tones BPF_1 and BPF_2, but under-predicts their harmonics, i.e., $nBPF_1$ and $nBPF_2$. Theses discrepancies may be explained by the following observation. The experimental data show a preponderance of tones at all shaft orders (recall Fig. 3) including both odd and even order ones. Yet, the theory only predicts even order tones (whether sum or difference ones) since the blade counts are even numbers. The paradox can be explained by noting that the theory (aerodynamic or acoustic) assumes that all of the blades in each rotor disc are identical and that they all experience the same loading time history over the course of each rotor revolution, but displaced spatially and temporally from that of the reference blade. This assumption results in acoustic energy being distributed amongst a subset of shaft orders. The actual blades in a given rotor disc, however, are not exactly the same as they are hand finished (they are made of composites) and they may not experience exactly the same time history due to inherent unsteadiness of the flow. Perhaps more importantly, the setting angles for the blades in a given rotor disc vary within a small range (typically in the ±0.1° range for F31/A31 (Ref. 9)) in a random fashion around the rotor disc thus slightly modifying the loading distribution on each blade. Therefore, for the actual rotors the precise phasing assumed by the theory does not occur, a consequence of which is that the acoustic energy is distributed amongst all shaft orders rather than just those singled out by the theory. As a result, some of the energy that according to the theory would have amassed in BPF_1 and BPF_2 tones is leaked into their harmonics $nBPF_1$ and $nBPF_2$. The same mechanism could explain the measurable levels for the difference tones (e.g., $2BPF_2$-$2BPF_1$, $3BPF_2$-$2BPF_1$, and $4BPF_2$-$3BPF_1$), for which the theory predicts very small radiation efficiencies and, thus, levels that would be too small to be visible in Figure 9.

Next, the variations of SPL on the sideline as a function of observer angle for the BPF_1, BPF_2, and BPF_1+BPF_2 tones are examined (see Fig. 11). While it is difficult to draw general conclusions about the data-theory comparisons on the absolute level basis, the trends in data appear to be reasonably well predicted except for the far upstream and far downstream angles for the BPF_1 and BPF_2 tones. It should be noted that the predicted rapid falloff of the SPL for BPF_1 and BPF_2 away from the vicinity of the respective planes of rotation (i.e., ~90° observer angle) is consistent with measured single rotation results. It is not clear then, why the measured blade passing tone levels for the individual rotors of F31/A31 should level off (or even increase) below about 70° and above approximately 130°.

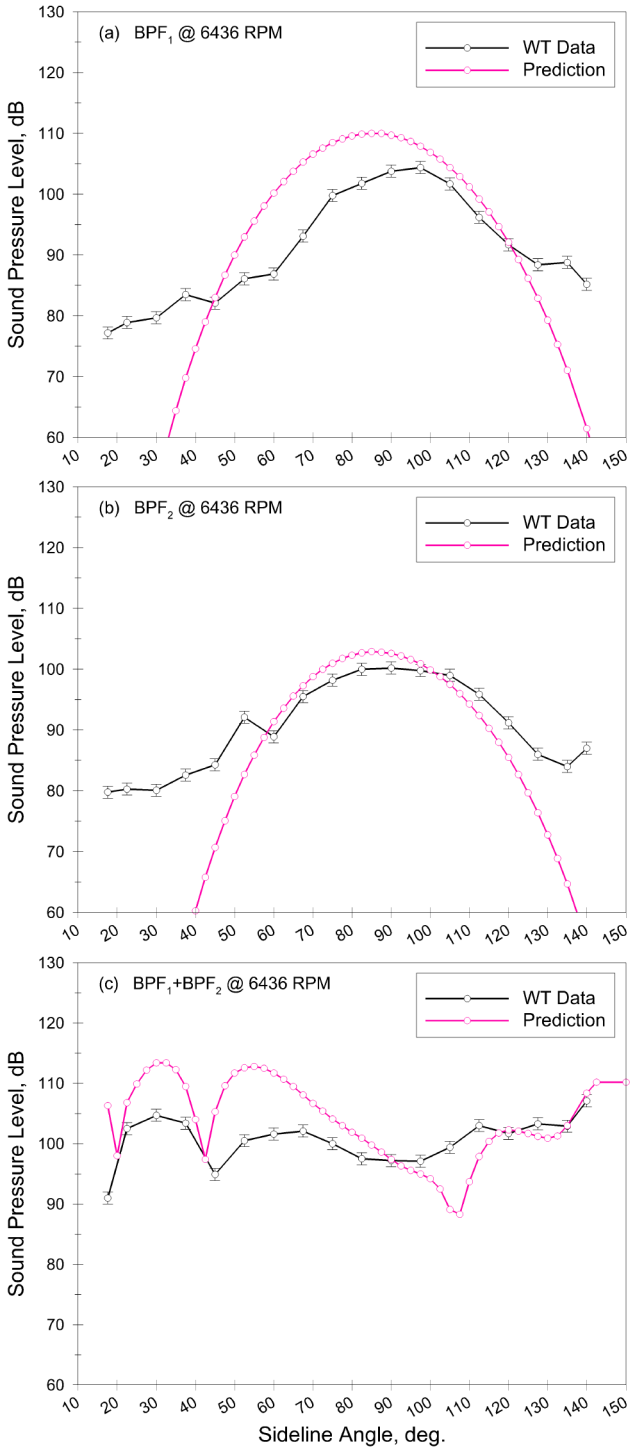

Figure 11.—Sideline variations of SPL as a function of observer angle for (a) BPF_1, (b) BPF_2, and (c) BPF_1+BPF_2 tones at the 6436 rpm condition.

[4] This was partially borne out by comparing the results to those from a single case that was run with a mesh resolution of 42 M grid points. However, the grid packing in the vicinity of the blade may be a more important factor than grid resolution alone.

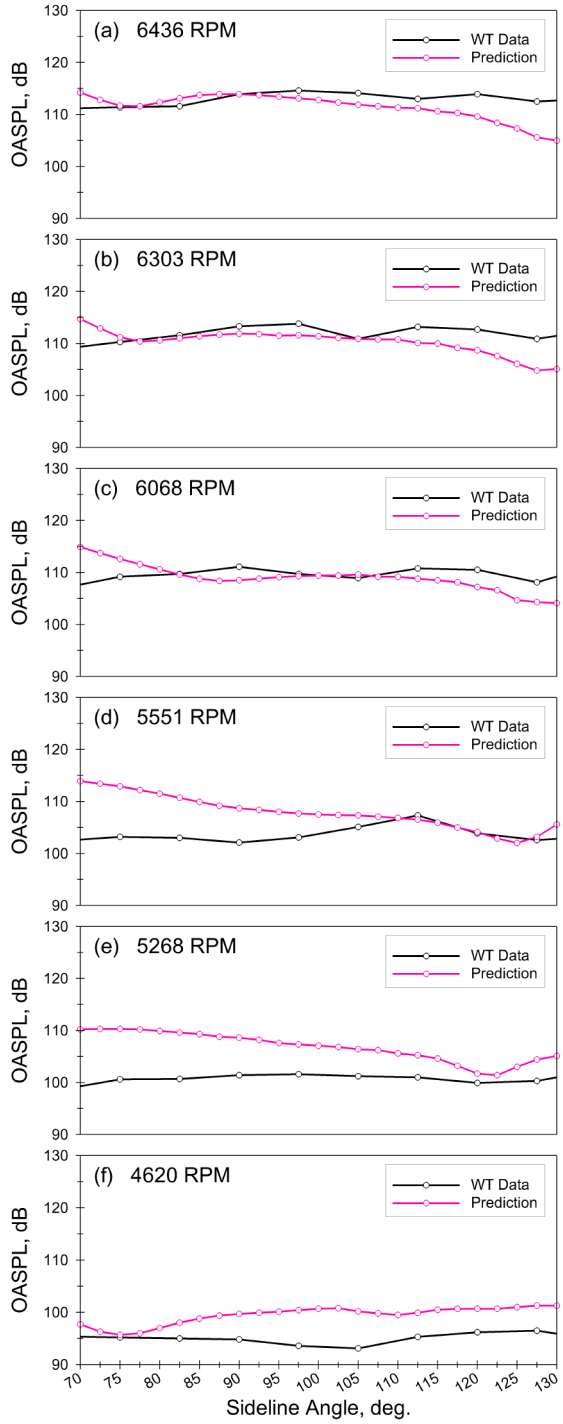

Figure 12.—Sideline variations of OASPL as a function of the observer angle on the sideline. Panes (a) to (f) show the variations of OASPL with tip speed. Comparisons for observer angles in the range 70° to 130° only are shown.

The data-theory comparisons look similar for the other tip speeds, so results corresponding to those presented in Figures 9 and 11 for lower tip speeds will not be presented here. Instead, the comparisons as a function of tip speed will be shown on the basis of the overall sound pressure level (OASPL). The principal reason for choosing the OASPL metric goes back to discussion earlier regarding the acoustic energy being distributed amongst all shaft order tones rather than just those orders that the theory predicts. It could be argued that in that sense the OASPL should be a good metric to use regardless of how the acoustic energy is distributed amongst the various tones. It should also be noted that since the measured levels include both tone and broadband content, it is necessary to subtract the broadband levels from the measured data before calculating the OASPL. Lastly, based on the discussion of the results in Figure 11, the OASPL comparisons will be restricted to the observer angles in the 70° to 130° range.

Figure 12 shows the dependence of the OASPL on the rotor tip speed. Both measured and predicted OASPLs are shown from the highest tip speed (6436 rpm) on the top of the figure to the lowest tip speed (4620 rpm) on the bottom of the figure. Generally speaking, the data-theory agreement is reasonable at the higher tip speeds, but it deteriorates as the tip speed is reduced. The basic trend of decreasing OASPL with decreasing tip speed in the measured data is captured by the theory though not uniformly for all observer angles in that the decrease in the predicted levels is slower than that in the measured data.

Conclusions

The results discussed in the previous section suggest that absolute level predictions on a tone-by-tone basis for open rotors (or any turbomachinery system, for that matter) may be out of reach using the existing suite of tools (i.e., CFD + acoustic analogy). This may be true even when more sophisticated numerical methods that directly compute the noise field from the field equations are brought to bear. This is a consequence of the fact that any model that assumes identical blades in each blade row, experiencing spatially- and temporally-shifted time histories, is incompatible with the real geometries, for which there always exist small manufacturing and installation variations as well as flow non-stationarity, which could in measurable ways alter the acoustic response of the blades. Nevertheless, the basic trends seem to be reasonably well predicted using the combination of CFD and acoustic analogy (specifically, in this case, FINE/Turbo and LINPROP). This is enough of a capability for analysis and optimization ultimately aimed at developing low-noise open rotor designs. It may also be possible to modify the existing noise models (such as that underlying the LINPROP code, for example) to accommodate small, randomized variations in the geometry and loading distributions on a blade-to-blade basis to mimic the real physics. The basic question here is whether the size of required variations to get more realistic tone spectra would turn out to be consistent with the expected variations in the actual geometries. It is the aim of a future study to investigate this approach and its consequences.

Appendix A—Acoustic Formulas

Taking advantage of the tonal nature of the sound field, one can write for the front rotor

$$p'(\underline{x},t)=\sum_{\ell=-\infty}^{\infty}p'_{T_\ell}(\underline{x})e^{-i\ell\Omega_1 t}+\sum_{\ell=-\infty}^{\infty}\sum_{k=-\infty}^{\infty}p'_{\mathcal{L}_{\ell,k}}(\underline{x})e^{-i\ell'\Omega_1 t} \tag{A.1a}$$

$$\ell'=\ell+kB_2\left(1+\Omega_2/\Omega_1\right)$$

where p'_{T_ℓ} and $p'_{\mathcal{L}_{\ell,k}}$ are the thickness and loading harmonic amplitudes. Based on Equation (1a), these are given by

$$p'_{T_\ell}(\underline{x})=\frac{\Omega_1}{2\pi}\times\int_0^{2\pi/\Omega_1}e^{i\ell\Omega_1 t}\left[\int_{-\infty}^{\infty}\int_{S_1}\rho_0\hat{v}_n\frac{D_0G}{Dt}ds(\underline{\hat{y}})d\tau\right]dt \tag{A.1b}$$

$$p'_{\mathcal{L}_{\ell,k}}(\underline{x})=-\frac{\Omega_1}{2\pi}\times\int_0^{2\pi/\Omega_1}e^{i\ell'\Omega_1 t}\left[\int_{-\infty}^{\infty}\int_{S_1}\hat{p}_k n_j\frac{\partial G}{\partial x_j}ds(\underline{\hat{y}})d\tau\right]dt \tag{A.1c}$$

Note that thickness noise involves only the rotational frequency of the front rotor since the surface (i.e., source) velocity $\hat{v}_n$ is not in any way influenced by the aft rotor. In contrast, loading noise depends not only on the front rotor rotational rate, but it is also affected by the rate at which the aft rotor blades pass by a given blade on the front rotor. In other words, the most general frequency of noise produced by the loading source depends on the combinations $\ell\Omega_1+kB_2\left(\Omega_1+\Omega_2\right)$. In the absence of the aft rotor, or when considering only the mean loading on the aft rotor, (i.e., $k=0$), the loading noise frequency reduces to the harmonics of the front rotor rotational frequency as expected.

In writing Equations (A.1b) and (A.1c), f_j in Equation (1a) has been replaced with its inviscid part pn_j, and the source coordinates have been switched from the stationary frame of reference to the ones in a rotating frame fixed to the rotor, i.e., $\underline{y}\to\underline{\hat{y}}$. The integration over the time dependant rotor surface $S_1(\tau)$ has been correspondingly replaced with integration over the time-independent rotor surface S_1, which denotes the aggregate surface of all the blades in the rotor disc. The transformation is length preserving and hence its Jacobian is unity. The source amplitudes $\hat{v}_n$ and $\hat{p}_k$ are also expressed in the blade fixed coordinate system.

Finally, the derivatives of the Green's function with respect to the source coordinate in Equation (1a) have been replaced with those with respect to the observer coordinates via

$$D_0G/D\tau=-D_0G/Dt$$
$$\partial G/\partial y_i=-\partial G/\partial x_i \tag{A.2}$$

Assuming that all the blades in the rotor disc are identical, the integration over the rotor surface S_1 can then be reduced to one over the surface of the reference blade S_{B_1}, since the contribution to the harmonic amplitude p'_{T_ℓ} from the q^{th} rotor blade is related to that from the reference (i.e., 0^{th}) blade through the spatial phase shift $e^{2\pi iq/B_1}$. Therefore, Equation (A.1b) can be rewritten as

$$p'_{T_\ell}=\frac{\Omega_1}{2\pi}\sum_{q=0}^{B_1-1}e^{2\pi i\ell q/B_1}\times\int_0^{2\pi/\Omega_1}e^{i\ell\Omega_1 t}\left[\int_{-\infty}^{\infty}\int_{S_{B_1}}\rho_0\hat{v}_n\frac{D_0G}{Dt}ds(\underline{\hat{y}})d\tau\right]dt \tag{A.3}$$

The summation over the blade index q is non-zero only when ℓ is an integer multiple of the blade count B_1. When $\ell=mB_1$ (m being an arbitrary integer), the summation is equal to B_1 times the contribution from the reference blade. Thus, Equation (A.3) reduces to

$$p'_{T_m}(\underline{x})=\frac{B_1\Omega_1}{2\pi}\times\int_0^{2\pi/\Omega_1}e^{imB_1\Omega_1 t}\left[\int_{-\infty}^{\infty}\int_{S_{B_1}}\rho_0\hat{v}_n\frac{D_0G}{Dt}ds(\underline{\hat{y}})d\tau\right]dt \tag{A.4}$$

which shows that thickness noise is produced at the harmonics of the blade passing frequency $B_1\Omega_1$.

The blade pressure loading $\hat{p}_k$ has, in general, the form

$$\hat{p}_k(\tau)=\hat{\hat{p}}_k e^{-ikB_2(\Omega_1+\Omega_2)\tau} \tag{A.5}$$

since, due to the influence of the adjacent blade row, the blade loading is always unsteady even in a rotor-fixed coordinate system.

Next, note that the loading distribution on the q^{th} blade at any time is related to the loading distribution on the reference

blade via the spatial phase shift $e^{2\pi iq/B_1}$, which accounts for the location shift, and the temporal phase shift $e^{2\pi iq/B_1(\Omega_1+\Omega_2)}$, which accounts for the time lead. Therefore, Equation (A.1c) can be rewritten as an integral over the reference blade surface as follows,

$$p'_{\mathcal{L}_{\ell,k}}(\underline{x}) = -\frac{\Omega_1}{2\pi}\sum_{q=0}^{B_1-1} e^{2\pi iq(\ell+kB_2)/B_1}\int_0^{2\pi/\Omega_1} e^{i\ell'\Omega_1 t} \times \left[\int_{-\infty}^{\infty}\int_{S_{B_1}} \hat{\hat{p}}_k e^{-ikB_2(\Omega_1+\Omega_2)\tau} n_j \frac{\partial G}{\partial x_j} ds(\underline{\hat{y}})\, d\tau\right] dt \tag{A.6}$$

where, as before, the summation over the blade index q is non-zero only when $\ell + kB_2$ is an integer multiple of the blade count B_1. When $\ell + kB_2 = mB_1$, the summation is equal to B_1 times the contribution from the reference blade. Thus, Equation (A.6) simplifies to

$$p'_{\mathcal{L}_{m,k}}(\underline{x}) = \frac{-B_1\Omega_1}{2\pi}\int_0^{2\pi/\Omega_1} e^{i(mB_1\Omega_1+kB_2\Omega_2)t} \times \left[\int_{-\infty}^{\infty}\int_{S_{B_1}} \hat{\hat{p}}_k e^{-ikB_2(\Omega_1+\Omega_2)\tau} n_j \frac{\partial G}{\partial x_j} ds(\underline{\hat{y}})\, d\tau\right] dt \tag{A.7}$$

which shows that, in general, loading noise is produced at the frequency combinations $mB_1\Omega_1 + kB_2\Omega_2$.

Next, the chain rule can be used to show that

$$\frac{\partial G}{\partial x_j} = \mathcal{D}_j G$$
$$\mathcal{D}_j = -\left[\frac{1}{c_0\kappa}\left(e_j - g_c M_{0_j}\right)\frac{\partial}{\partial t} + \frac{1}{\kappa^2 R}\left(\beta_0^2 e_j + M_{0_R} M_{0_j}\right)\right] \tag{A.8}$$

which, in turn, can be used to remove the spatial derivatives in Equations (A.4) and (A.7). Afterwards, the integrations over t can be easily carried out since they involve Dirac delta functions. The results are

$$p'_{\mathcal{T}_m}(\underline{x}) = \frac{B_1\Omega_1}{8\pi^2}\int_0^{2\pi/\Omega_1}\int_{S_{B_1}} \left(\sum_{n=1}^{2}\frac{\mathcal{Q}^{(n)}_{\mathcal{T}_m}}{R^n}\right) \times e^{imB_1\Omega_1(\tau+g_cR/c_0)} ds(\underline{\hat{y}})\, d\tau \tag{A.9a}$$

$$p'_{\mathcal{L}_{m,k}}(\underline{x}) = \frac{B_1\Omega_1}{8\pi^2}\int_0^{2\pi/\Omega_1}\int_{S_{B_1}} \left(\sum_{n=1}^{2}\frac{\mathcal{Q}^{(n)}_{\mathcal{L}_{m,k}}}{R^n}\right) \times e^{i(mB_1\Omega_1+kB_2\Omega_2)(\tau+g_cR/c_0)} e^{-ikB_2(\Omega_1+\Omega_2)\tau} ds(\underline{\hat{y}})\, d\tau \tag{A.9b}$$

where $\mathcal{Q}^{(1)}_{\mathcal{T}_m}$ and $\mathcal{Q}^{(2)}_{\mathcal{T}_m}$ are the farfield and nearfield thickness source amplitudes, and $\mathcal{Q}^{(1)}_{\mathcal{L}_{m,k}}$ and $\mathcal{Q}^{(2)}_{\mathcal{L}_{m,k}}$ are the farfield and nearfield loading source amplitudes. These are given by Equation (A.9c).

Note that, the limits of integration over τ in Equation (A.9a) and (A.9b) have been set to $(0, 2\pi/\Omega_1)$, since one period of the observer time maps exactly into one period of the source time. In what follows it will be assumed that the mean flow is aligned with the open rotor axis, i.e., $(M_{0_1}, 0, 0)$.

$$\mathcal{Q}^{(1)}_{\mathcal{T}_m} = -\frac{1}{\kappa^2} imB_1\Omega_1\rho_0\hat{v}_n \times \left[1 - \frac{1}{\kappa}M_{0_j}\left(e_j - g_c M_{0_j}\right)\right]$$

$$\mathcal{Q}^{(2)}_{\mathcal{T}_m} = -\frac{1}{\kappa^3}\rho_0\hat{v}_n M_{0_j}\left(\beta_0^2 e_j + M_{0_R} M_{0_j}\right)$$

$$\mathcal{Q}^{(1)}_{\mathcal{L}_{m,k}} = -\frac{1}{c_0\kappa^2} i\left(mB_1\Omega_1 + kB_2\Omega_2\right) \times \hat{\hat{p}}_k n_j\left(e_j - g_c M_{0_j}\right) \tag{A.9c}$$

$$\mathcal{Q}^{(2)}_{\mathcal{L}_{m,k}} = \frac{1}{\kappa^3}\hat{\hat{p}}_k n_j\left(\beta_0^2 e_j + M_{0_R} M_{0_j}\right)$$

Grouping terms together and introducing a change of variable from τ to a new variable θ, both the thickness and loading terms can be cast in the form given by

$$p'(\underline{x}) = \frac{B_1}{8\pi^2}\sum_{n=1}^{2}\int_{S_{B_1}} e^{-i\lambda\Psi}\mathcal{I}_n(\hat{\underline{y}})\,ds(\hat{\underline{y}})$$
$$\mathcal{I}_n = \int_0^{2\pi}\frac{\mathcal{Q}^{(n)}(\theta)}{R^n(\theta)}e^{\lambda\Phi(\theta)}d\theta \tag{A.10a}$$

$$\theta = \Omega_1\tau + \varphi_s - \varphi$$
$$\Phi(\theta) = i\left(\theta + a_s\sqrt{1-b_s\cos\theta}\right) \tag{A.10b}$$
$$b_s = \frac{2rr_s}{\chi_s^2 + r^2 + r_s^2},\quad \chi_s = \frac{1}{\beta_{0_1}}(x_1 - \hat{y}_1)$$

where for thickness noise[5]

$$\lambda = mB_1$$
$$a_s = \frac{M_{\mathrm{tip}_1}}{\beta_{0_1}}\sqrt{\chi_s^2 + r^2 + r_s^2}$$
$$\Psi = \frac{1}{\beta_{0_1}}M_{\mathrm{tip}_1}M_{0_1}\chi_s + \varphi_s - \varphi \tag{A.10c}$$
$$M_{\mathrm{tip}_1} = \frac{\Omega_1 R_{\mathrm{tip}_1}}{c_0}$$

and for the loading noise

$$\lambda = mB_1 - kB_2$$
$$a_s = \frac{\eta_{\mathrm{CRF}}M_{\mathrm{tip}_1}}{\beta_{0_1}}\sqrt{\chi_s^2 + r^2 + r_s^2}$$
$$\Psi = \frac{\eta_{\mathrm{CRF}}}{\beta_{0_1}}M_{\mathrm{tip}_1}M_{0_1}\chi_s + \varphi_s - \varphi \tag{A.10d}$$
$$\eta_{\mathrm{CRF}} = \frac{mB_1 + kB_2\Omega_2/\Omega_1}{mB_1 - kB_2}$$

Here η_{CRF} is a factor denoting the influence of the counter-rotation kinematics on the loading noise. Note that for $k = 0$, i.e., when considering the influence of only the mean loading from the aft rotor on the noise of the front rotor, Equations (A.10c) and (A.10d) have identical forms, which is to say that the thickness and loading noise components have the same frequency content. This result is in agreement with the isolated rotor results developed in Reference 7. In general, however, loading noise for a given rotor is strongly influenced by its neighbor. It should be noted that in circumstances for which $mB_1 = kB_2$, the loading term parameters have the following simpler forms

$$\Phi(\theta) = ia_s\sqrt{1-b_s\cos\theta}$$
$$\lambda = mB_1$$
$$a_s = \frac{\eta_{\mathrm{CRF}}M_{\mathrm{tip}_1}}{\beta_{0_1}}\sqrt{\chi_s^2 + r^2 + r_s^2} \tag{A.10e}$$
$$\Psi = \frac{\eta_{\mathrm{CRF}}}{\beta_{0_1}}M_{\mathrm{tip}_1}M_{0_1}\chi_s$$
$$\eta_{\mathrm{CRF}} = 1 + \frac{\Omega_2}{\Omega_1}$$

As shown in Reference 7, the integral $\mathcal{I}_n$ in Equation (A.10a) can be accurately estimated using the method of steepest descent when the parameter λ is large which is the generally the case due to the large blade counts of modern open rotors. The essential steps are twofold: (1) conformably map the phase function Φ into a suitably constructed polynomial which facilitates the analysis immensely; (2) extend the domain of analysis to the complex domain through the change of variable $\nu = \theta + i\sigma$ which allows the path of integration to be deformed into appropriate steepest descent paths. In the neighbourhoods of the saddle points of these paths, the integral $\mathcal{I}_n$ can then be accurately estimated using closed form analytical expressions. The intermediate steps are described in detail in Reference 7. The final result for a generic source term is given by

$$\mathcal{I}_n \simeq 2\pi i e^{\lambda\mu}\left\{d_{0,n}\frac{Ai\left(\lambda^{2/3}\gamma^2\right)}{\lambda^{1/3}} + d_{1,n}\frac{Ai'\left(\lambda^{2/3}\gamma^2\right)}{\lambda^{2/3}}\right\}$$
$$d_{0,n} = \frac{\Gamma_n(\gamma) + \Gamma_n(-\gamma)}{2}$$
$$d_{1,n} = \frac{\Gamma_n(\gamma) - \Gamma_n(-\gamma)}{2\gamma}$$
$$\mu = \frac{1}{2}\left[\Phi\left(\nu^+\right) + \Phi\left(\nu^-\right)\right] \tag{A.11}$$
$$\gamma^3 = \frac{3}{4}\left[\Phi\left(\nu^+\right) - \Phi\left(\nu^-\right)\right]$$
$$\Gamma_n(\zeta) = \frac{\mathcal{Q}^{(n)}\left[\nu(\zeta)\right]}{R^n\left[\nu(\zeta)\right]}\frac{d\nu}{d\zeta}$$
$$\frac{d\nu}{d\zeta} = \frac{\gamma^2 - \zeta^2}{\Phi'\left[\nu(\zeta)\right]}$$

[5] The definition of the parameter a_s as given in the Reference 7 is incorrect.

where $\nu^{\pm}$ denote the location of the saddle points in the complex plane and μ, γ, and Γ_n are parameters that define the conformal map. $d_{0,n}$, and $d_{1,n}$ are the source amplitudes at the saddle points. Note that the actual values of these parameters depend on whether thickness noise or loading noise is being considered.

The Airy function Ai and its derivative Ai' provide an accurate asymptotic approximation to the integral $\mathcal{I}_n$. The approximation is uniformly valid at subsonic, transonic, and supersonic tip speeds. It is also uniformly valid whether the observer is in the nearfield or farfield. The approximation is formally accurate for large values of the parameter λ, but it turns out to be surprisingly accurate even for values of λ as low as 2.

With the integral $\mathcal{I}_n$ computed, the integration over the blade surface S_{B_1} in Equation (A.10a) can now be carried out to compute the harmonic amplitudes of the thickness and loading noise sources. For general blade shapes, this integrals is not tractable analytically, but can be easily computed using a quadrature scheme by dividing the blade surface into small elements over which the integral can be accurately estimated (see Ref. 7). For the acoustic results presented in this paper, the surface grid generated as part of the FINE/Turbo simulations was used in the surface quadrature calculations.

References

1. Hager, R., D., and Vrable, D., 1988, "Advanced Turboprop Project," NASA SP-495.
2. Van Zante, D., E., Gazzaniga, J., A., Elliott, D., M., and Woodward, R., P., 2011, "An Open Rotor Test Case: F31/A31 Historical Baseline Blade Set," *20th ISABE Conference*, Gothenburg, Sweden, paper no. ISABE-2011-1310.
3. Farassat, F., Dunn, M., H., Tinetti, A. F., and Nark, D., M., 2009, "Open Rotor Noise Prediction Methods at NASA Langley–A Technology Review," AIAA Paper 2009-3133, *15th AIAA/CEAS Aeroacoustics Conference*, Miami, Florida.
4. Brès, G., A., Brentner, K., S., Perez, G., and Jones, H., E., 2004, "Maneuvering Rotorcraft Noise Prediction," *J. of Sound and Vibration*, Vol. 275, Issues 3-5, pp. 719-738.
5. Hanson, D., B., 1985, "Noise of Counter-Rotation Propellers," *Journal of Aircraft*, Vol. 22, No. 7, pp. 609-617.
6. Parry, A., B., 1988, "Theoretical Prediction of Counter-Rotating Propeller Noise," *Ph.D. Dissertation, Dept. of Applied Mathematical Studies, University of Leeds*.
7. Envia, E., 1994, "Asymptotic Theory of Supersonic Propeller Noise," *AIAA Journal*, Vol. 32, No. 2, pp. 239-246.
8. He, L. and Ning, W., 1998, "Efficient Approach for Analysis of Unsteady Viscous Flows in Turbomachines," *AIAA Journal*, Vol. 36, No. 11, pp. 2005-2011.
9. Van Zante, D., E., Private communications.

REPORT DOCUMENTATION PAGE			Form Approved OMB No. 0704-0188

1. REPORT DATE *(DD-MM-YYYY)*	2. REPORT TYPE	3. DATES COVERED *(From - To)*
01-10-2012	Technical Memorandum	

4. TITLE AND SUBTITLE
Open Rotor Aeroacoustic Modelling

5a. CONTRACT NUMBER

5b. GRANT NUMBER

5c. PROGRAM ELEMENT NUMBER

6. AUTHOR(S)
Envia, Edmane

5d. PROJECT NUMBER

5e. TASK NUMBER

5f. WORK UNIT NUMBER
WBS 561581.02.08.03.45.02.04

7. PERFORMING ORGANIZATION NAME(S) AND ADDRESS(ES)
National Aeronautics and Space Administration
John H. Glenn Research Center at Lewis Field
Cleveland, Ohio 44135-3191

8. PERFORMING ORGANIZATION REPORT NUMBER
E-18485

9. SPONSORING/MONITORING AGENCY NAME(S) AND ADDRESS(ES)
National Aeronautics and Space Administration
Washington, DC 20546-0001

10. SPONSORING/MONITOR'S ACRONYM(S)
NASA

11. SPONSORING/MONITORING REPORT NUMBER
NASA/TM-2012-217740

12. DISTRIBUTION/AVAILABILITY STATEMENT
Unclassified-Unlimited
Subject Categories: 02, 64, and 71
Available electronically at http://www.sti.nasa.gov
This publication is available from the NASA Center for AeroSpace Information, 443-757-5802

13. SUPPLEMENTARY NOTES

14. ABSTRACT
Owing to their inherent fuel efficiency, there is renewed interest in developing open rotor propulsion systems that are both efficient and quiet. The major contributor to the overall noise of an open rotor system is the propulsor noise, which is produced as a result of the interaction of the airstream with the counter-rotating blades. As such, robust aeroacoustic prediction methods are an essential ingredient in any approach to designing low-noise open rotor systems. To that end, an effort has been underway at NASA to assess current open rotor noise prediction tools and develop new capabilities. Under this effort, high-fidelity aerodynamic simulations of a benchmark open rotor blade set were carried out and used to make noise predictions via existing NASA open rotor noise prediction codes. The results have been compared with the aerodynamic and acoustic data that were acquired for this benchmark open rotor blade set. The emphasis of this paper is on providing a summary of recent results from a NASA Glenn effort to validate an in-house open noise prediction code called LINPROP which is based on a high-blade-count asymptotic approximation to the Ffowcs-Williams Hawkings Equation. The results suggest that while predicting the absolute levels may be difficult, the noise trends are reasonably well predicted by this approach.

15. SUBJECT TERMS
Aerodynamic noise; Propeller noise; Noise modeling

16. SECURITY CLASSIFICATION OF:			17. LIMITATION OF ABSTRACT	18. NUMBER OF PAGES	19a. NAME OF RESPONSIBLE PERSON
a. REPORT	b. ABSTRACT	c. THIS PAGE			STI Help Desk (email:help@sti.nasa.gov)
U	U	U	UU	22	19b. TELEPHONE NUMBER *(include area code)* 443-757-5802